Late Holocene uplift of Rhodes, Greece: evidence for a large tsunamigenic earthquake and the implications for the tectonics of the eastern Hellenic Trench System

Andy Howell,[1] James Jackson,[1] Philip England,[2] Thomas Higham[3] and Costas Synolakis[4,5]

[1]*COMET, Department of Earth Sciences, University of Cambridge, Bullard Labs, Madingley Road, Cambridge* CB3 0EZ*, United Kingdom.*
E-mail: arh79@cam.ac.uk
[2]*Department of Earth Sciences, University of Oxford, South Parks Road, Oxford* OX1 3AN*, United Kingdom*
[3]*Oxford Radiocarbon Accelerator Unit, University of Oxford, Oxford* OX1 3QY*, United Kingdom*
[4]*Department of Environmental Engineering, Technical University of Crete, Chania, Greece*
[5]*Viterbi School of Engineering, University of Southern California, Los Angeles, CA* 90089-2531*, USA*

SUMMARY

Several large earthquakes in the Hellenic subduction zone have been documented in historical records from around the eastern Mediterranean, but the relative seismic quiescence of the region over the period of instrumental observation means that the exact locations of these earthquakes and their tectonic significance are not known. We present AMS radiocarbon dates from uplifted late Holocene palæoshorelines from the island of Rhodes, showing that uplift is most consistent with a single large ($M_W \geq 7.7$) reverse-faulting earthquake between about 2000 BC and 200 BC. Analysis of the uplift treating the earthquake as a dislocation in an elastic half-space shows a predominantly reverse-faulting event with a slip vector oblique to the direction of convergence between Rhodes and Nubia. We suggest that the fault responsible for the uplift dips at an angle of 30–60° above the more gently dipping oblique subduction interface. The highly oblique convergence across the eastern Hellenic plate boundary zone appears to be partitioned into reverse slip on faults that strike parallel to the boundary and strike-parallel or oblique slip on the subduction interface. Hydrodynamical simulation of tsunami propagation from a range of tectonically plausible sources suggests that earthquakes on the fault uplifting Rhodes represent a significant tsunami hazard for Rhodes and SW Turkey, and also possibly for Cyprus and the Nile Delta.

Key words: Tsunamis; Subduction zone processes; Continental margins: convergent; Tectonics and landscape evolution.

1 INTRODUCTION

Historical records for cities across the eastern Mediterranean document widespread and catastrophic earthquake and tsunami damage on several occasions during the past 2000 yr, most notably in AD 365 and AD 1303 (Guidoboni & Comastri 1997; Shaw *et al.* 2008; Ambraseys 2009; Ambraseys & Synolakis 2010; Stiros 2010). Alexandria and the rest of the Nile Delta were flooded extensively by these two tsunamis, which are suggested by analyses of damage distributions to have been caused by earthquakes in the Hellenic subduction zone (Ambraseys 2009).

Palæoshorelines in SW Crete record up to 9 m of late-Holocene uplift, consistent with a single earthquake in AD 365 (Pirazzoli *et al.* 1996; Shaw *et al.* 2008; Stiros 2010). Shaw *et al.* (2008) show that the best-fitting earthquake source for this event is a reverse fault outcropping at a prominent bathymetric escarpment known as the

Hellenic Trench. It has been suggested that other deep linear features within the Hellenic plate boundary zone, such as the Pliny and Strabo Trenches (Fig. 1; Emery *et al.* 1966), may also be the surface projections of faults (e.g. McKenzie 1978; Mascle *et al.* 1986; Huguen *et al.* 2001; Özbakır *et al.* 2013; Gallen *et al.* 2014). It is therefore important for the assessment of earthquake and tsunami hazard in the eastern Mediterranean to determine whether these features represent seismically active faults and, if so, what magnitude of earthquakes they are capable of generating.

This study focuses on a set of uplifted late Holocene shorelines on Rhodes, previously attributed to differential motions between several small crustal blocks (Pirazzoli *et al.* 1989), or alternatively to one large-magnitude earthquake on an offshore fault (Kontogianni *et al.* 2002). We constrain the timing of uplift using radiocarbon dating and refine the uplift distribution suggested by Kontogianni *et al.* (2002) to allow for possible later
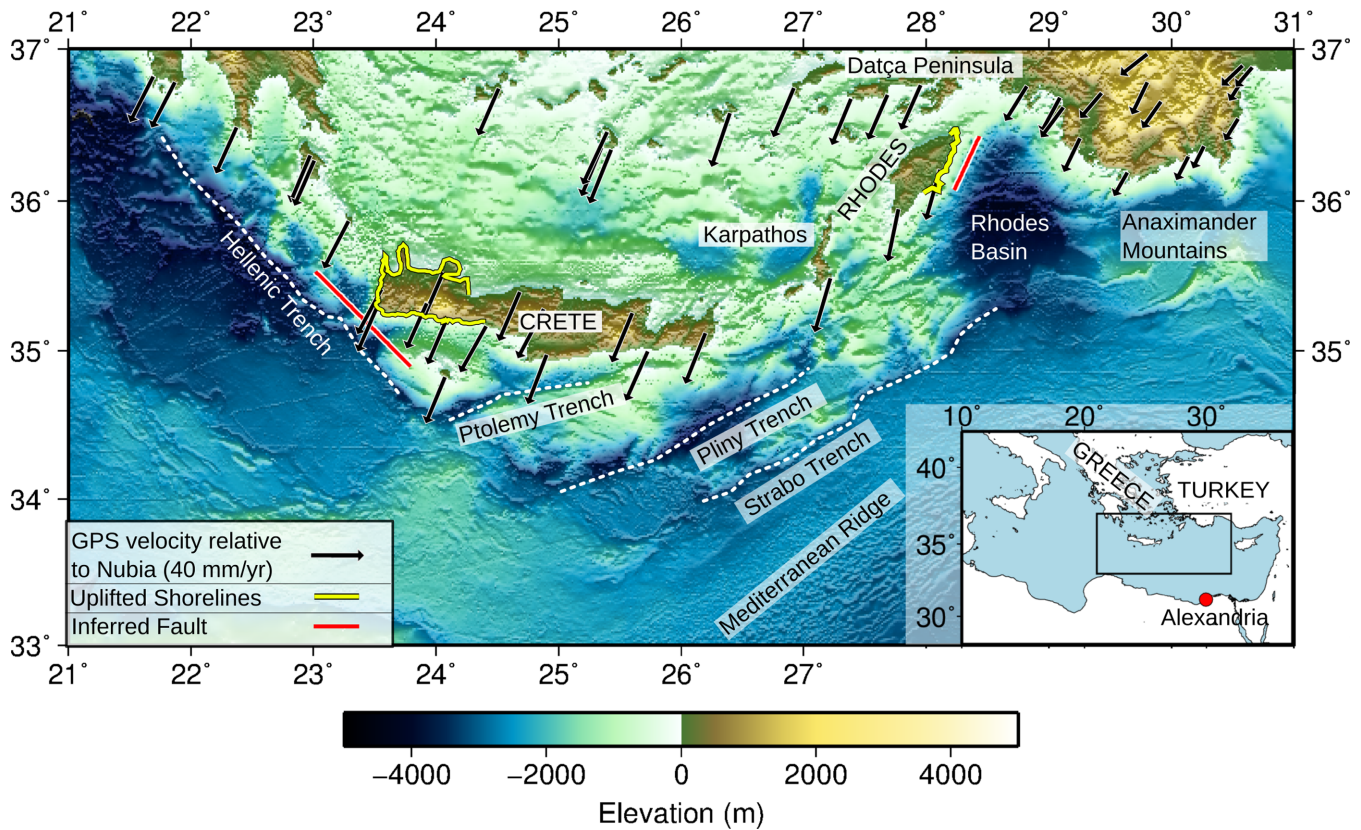

Figure 1. Tectonic and bathymetric setting of the Hellenic Trench System. Dashed white lines mark steep linear escarpments. Black arrows show GPS velocities for the Aegean (Nocquet 2012; Tiryakioğlu *et al.* 2013), rotated into a Nubian reference frame using the pole of DeMets *et al.* (2010). Yellow coastlines show the principal regions of late Holocene uplift on Crete and Rhodes discussed in the text. Red lines show the approximate lengths and locations of the faults inferred by Shaw *et al.* (2008) and this study (near Crete and Rhodes, respectively). Bathymetry is from the SRTM30+ (Becker *et al.* 2009) and is illuminated from the south.

subsidence due to normal faulting in NW Rhodes. We examine the constraints on the strike, dip and slip vector of a fault that could be responsible for the observed uplift, which also allows us to consider the kinematics of the oblique convergence between Rhodes and the eastern Mediterranean seafloor (part of the Nubian plate).

2 TECTONIC SETTING OF RHODES

In the Hellenic plate boundary zone, oceanic Nubian lithosphere is subducted beneath Eurasian continental lithosphere, which extends at about 30 mm yr^{-1} (Nocquet 2012) so that the motion of the Aegean relative to Nubia is subperpendicular to the strike of the subduction zone west of 24°E, but becomes increasingly oblique towards the eastern end of the zone, at Rhodes (Chaumillon & Mascle 1997; Fig. 1). The presence of N–S normal-fault scarps across Crete and the Peloponnese and the strikes of faults offshore from Crete (e.g. Huchon *et al.* 1982; Armijo *et al.* 1992; Caputo *et al.* 2010) suggest arc-parallel extension in the overriding Aegean lithosphere, a suggestion that is supported by data from GPS and earthquake slip vectors (e.g. Floyd *et al.* 2010; Reilinger *et al.* 2010; Shaw & Jackson 2010; Nocquet 2012).

Where the rate of convergence is fastest (close to Crete), it appears to be at least 80 per cent aseismic (e.g. Jackson & McKenzie 1988; Shaw & Jackson 2010; Vernant *et al.* 2014). Shaw *et al.* (2008) showed that the predominantly aseismic subduction is consistent with the occurrence of rare great earthquakes at the plate boundary

if the fault which ruptured in AD 365 is not the subduction interface, but a reverse fault within the overriding crust. This conclusion is consistent with other interpretations of the steep bathymetric escarpments of the Hellenic Trench System as the surface projections of faults (e.g. Le Pichon *et al.* 1979; Chaumillon & Mascle 1997; Huguen *et al.* 2001; Özbakır *et al.* 2013; Gallen *et al.* 2014).

Rhodes lies beyond the eastern termination of the steep, NE-trending bathymetric escarpments known as the Pliny and Strabo Trenches. The SE margin of Rhodes is bounded by a steep bathymetric escarpment trending 025° (Kontogianni *et al.* 2002; Becker *et al.* 2009), with seismic reflection evidence for NW-dipping reverse faults between Rhodes and the Rhodes Basin (Woodside *et al.* 2000; Hall *et al.* 2009). Further to the SE a series of bathymetric highs, the Anaximander Mountains, probably form by active reverse faulting (Aksu *et al.* 2009, 2014). Reflection seismic data show numerous small folds and faults on the eastern side of the Rhodes Basin and in the Anaximander Mountains (ten Veen *et al.* 2004; Aksu *et al.* 2009; Hall *et al.* 2009).

3 OBSERVATIONS OF UPLIFT RELATIVE TO SEA LEVEL

3.1 Mode of uplift

Uplifted palæoshorelines in the form of prominent notches are visible in limestone cliffs along much of the SE coast of Rhodes (Figs 2a–b and 3), and radiocarbon dating of marine fauna shows them to be late Holocene in age (Pirazzoli *et al.* 1989; Section 3.3,
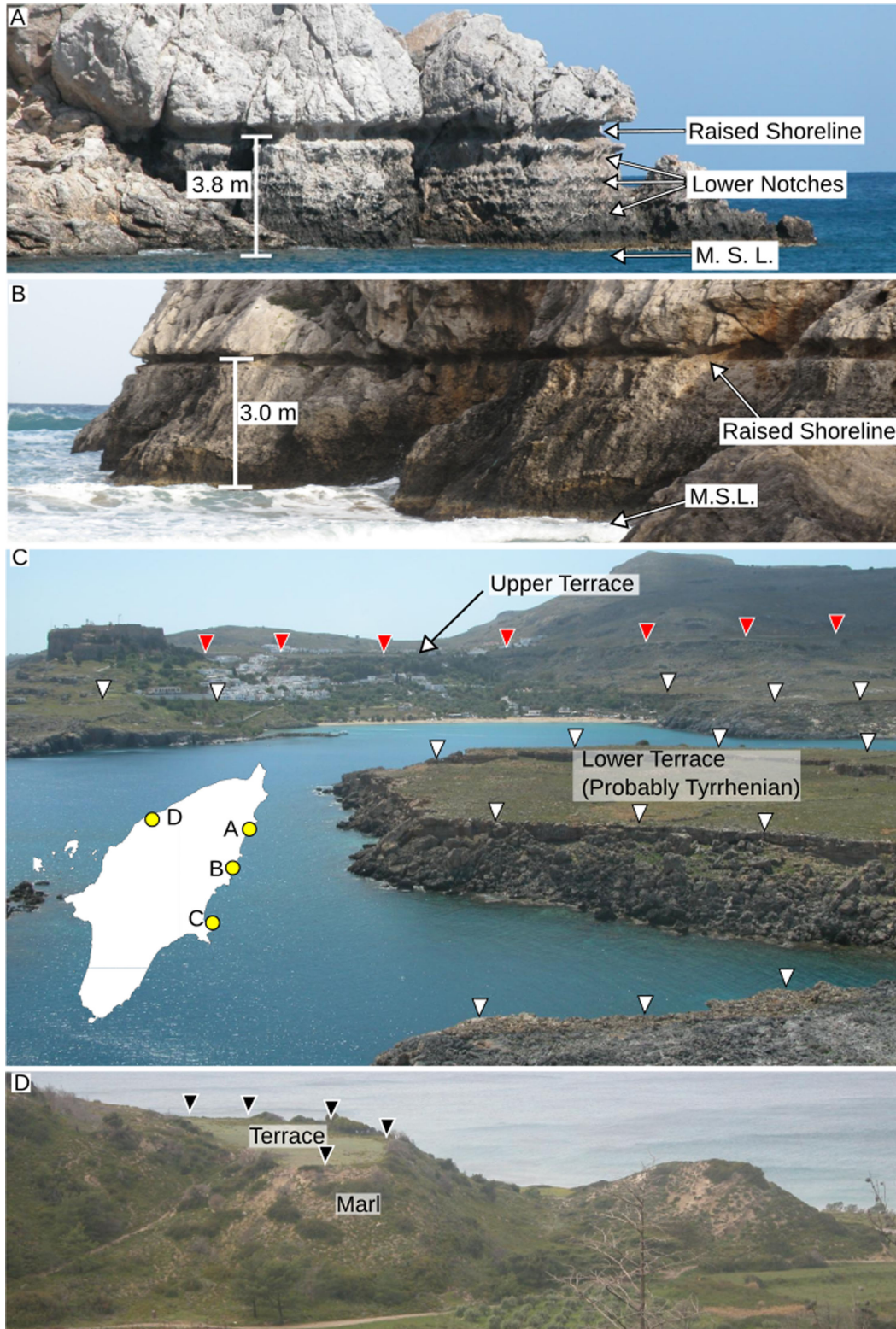
Figure 2. Geomorphological features associated with late Holocene and Quaternary uplift of Rhodes. Panels (a) and (b) show uplifted notches on the E coast at Traganou (36.31°N) and Tzambika (36.22°N), respectively. Panels (c) and (d) show Quaternary marine terraces at Lindos (36.10°N, view W) and Kamiros (36.33°N, NW coast, view W). Terrace levels are marked by coloured triangles.

this study). The notches reach a maximum of 3.8 m above the present-day mean sea level (MSL) at Ladikou (36.32°N, 28.21°E) and approach zero elevation SW of Lindos (36.09°N, 28.09°E; Fig. 3b). Quaternary marine terraces (Figs 2c and d) exist around the E and NW coasts of the island, at heights of up to 200 m above MSL adjacent to the notched Holocene palæoshorelines (Gauthier 1979; Kontogianni *et al.* 2002). In addition, there are terraces at 10–20 m elevation in the very S of Rhodes, where
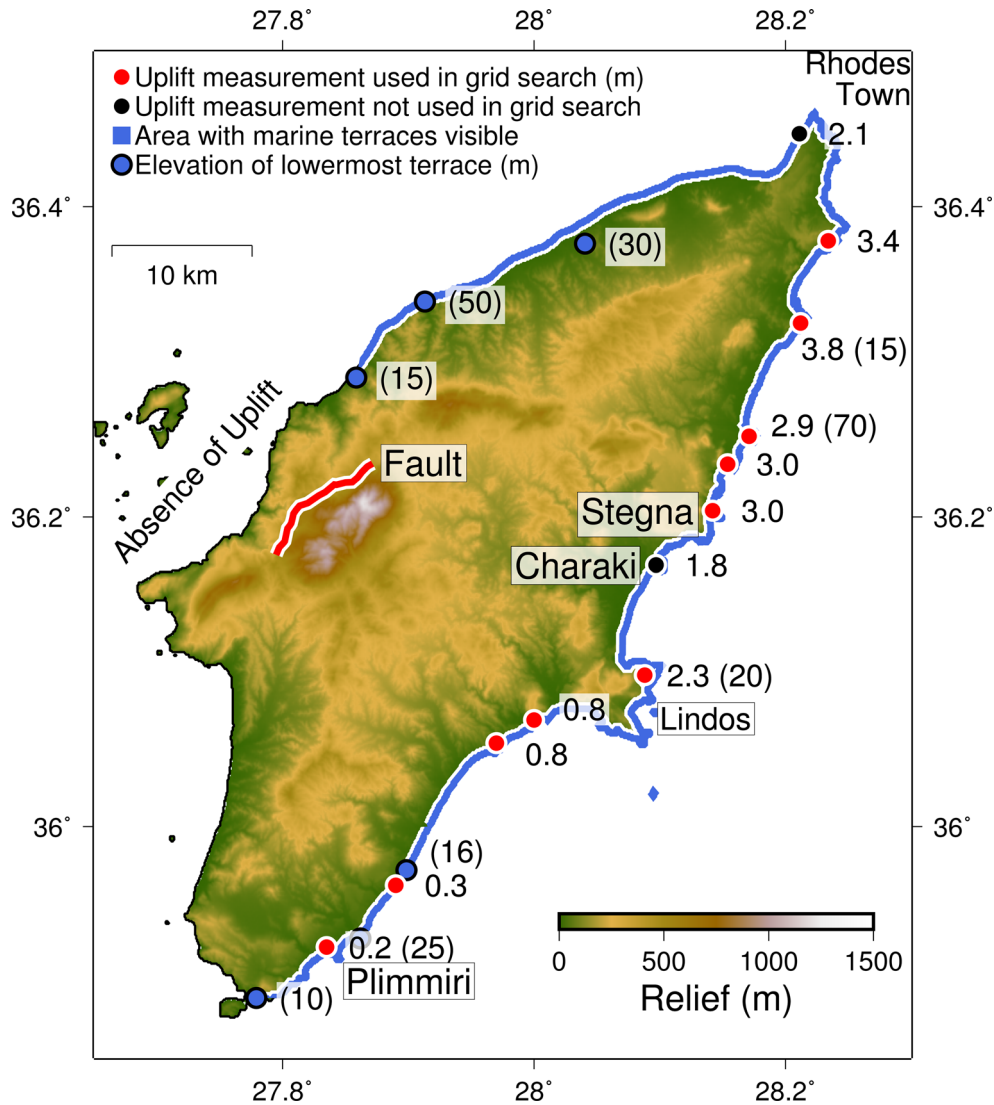
Figure 3. The uplift distribution used by Kontogianni *et al.* (2002), marked by red and black circles. We do not use the uplift measurements at Charaki and Rhodes Town marked by black circles for the reasons discussed in Section 3.2. The solid blue line marks the region of the coast where uplifted marine terraces are seen, and blue dots mark reported elevations of the lowest terrace (Gauthier 1979; Titschack *et al.* 2008). The region where any late Holocene uplift might be expected to be observed in the resistant limestone cliffs, if it were present, is marked by 'absence of uplift'. The trace of the fault in Fig. 4(b) is marked by the solid red line. Topography is SRTM (Farr *et al.* 2007).

Holocene uplift is small (Gauthier 1979; Titschack *et al.* 2008). The co-location of the uplifted palæoshorelines and the marine terraces suggests that uplift of Rhodes is tectonic in origin, and has continued through the Quaternary.

The late-Quaternary uplift of Rhodes could plausibly be caused by one of three processes: (1) infrequent large earthquakes (as suggested for Crete by Shaw *et al.* 2008); (2) frequent small earthquakes (Pirazzoli *et al.* 1989; Caputo *et al.* 2010); and (3) continuous gradual uplift, possibly related to sedimentary underplating.

At all of the localities where notches are observed, there is a notch at the height indicated in Fig. 3(b) and also a notch or algal encrustation at the present-day MSL; but at some localities (such as Traganou, 36.31°N, 28.19°E; Fig. 2a), smaller notches are observed between these two heights. Their presence was used by Pirazzoli *et al.* (1989) to infer differential uplift and subsidence of crustal blocks over multiple earthquakes, but similar multiple notches that do not represent multiple earthquakes are observed on uplifted coastlines throughout the eastern Mediterranean. In the

Gulf of Corinth, the ages of these lower notches do not match the times of historical earthquakes, and notch formation has been attributed to climatic processes (Cooper *et al.* 2007) or earthquake clustering (Boulton & Stewart 2015). On Crete, the uplift in AD 365 (up to 9 m; Shaw *et al.* 2008) is much greater than the spacing between the lower notches, so their origin there is probably unrelated to coseismic uplift.

On Rhodes itself, the lack of continuity along strike of these lower notches suggests that they may have a local origin, reflecting variable conditions of lithology or chemical and biological dissolution. Furthermore, neither our radiocarbon dates (Section 3.3) nor those of Pirazzoli *et al.* (1989) show any correlation between sample age and height, as might be expected for gradual uplift. The samples that yield evidence of uplift in the interval 4000–2000 BP cover the full elevation range of the uplifted Holocene shorelines (Table 1), suggesting a single uplift event. Finally, the correlated terraces at Lindos and Plimmiri (which are probably of Tyrrhenian age; Gauthier 1979; Titschack *et al.* 2008, Fig. 3) are at similar elevations
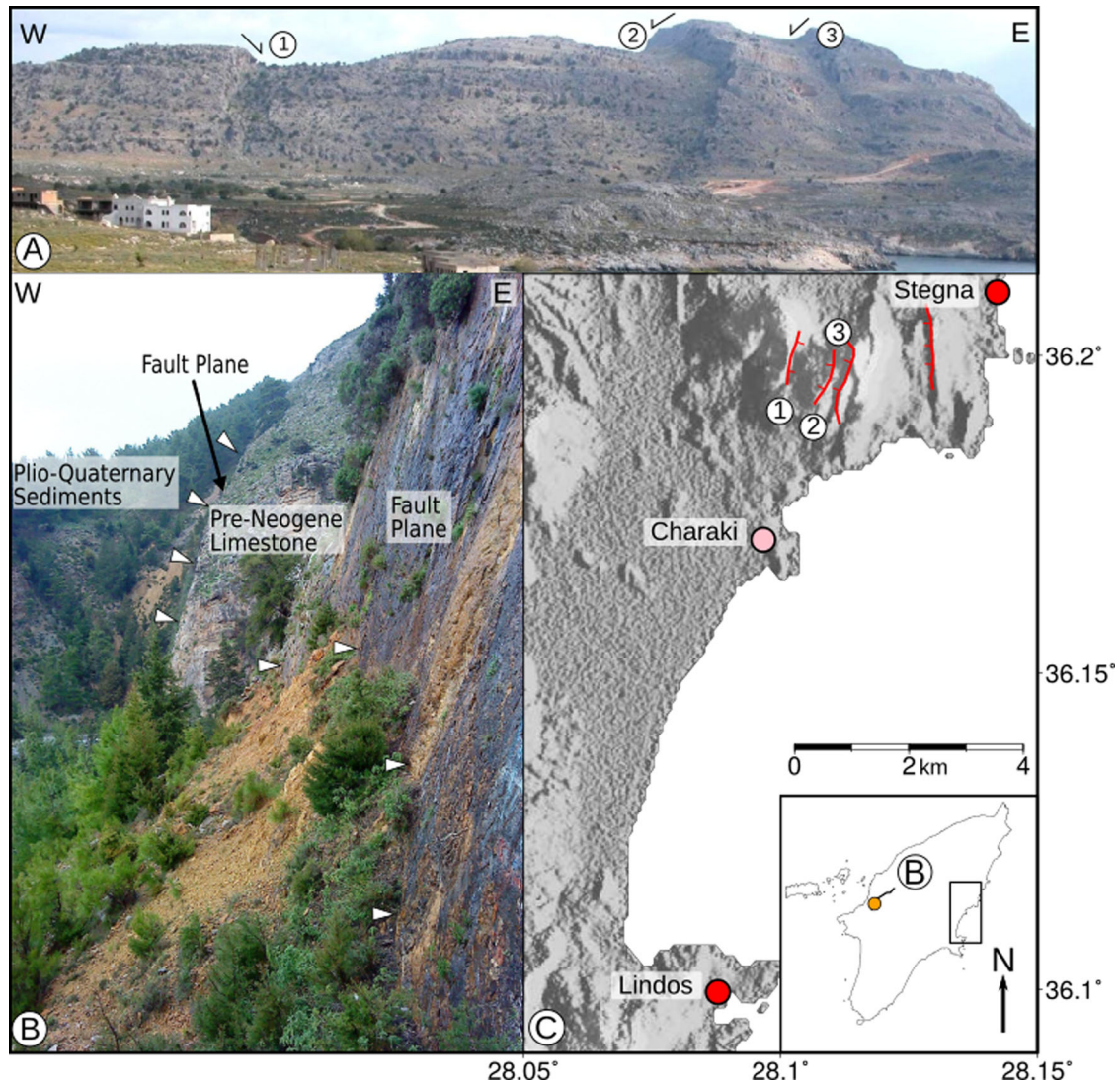
Figure 4. Relationship of normal faults observed by Gauthier (1979) to sites where uplift of palæoshorelines was measured. Faults are marked by arrows showing direction of slip in (a) and red lines with tick-marks on the hanging wall side in (c). Points where measurements of palæoshoreline uplift were recorded are marked by filled circles, colour coded according to Fig. 6. The photo in (a) was taken from Charaki, facing NNE. The topography in (c) is from SRTM X-band data (Farr *et al.* 2007). Panel (b) shows a photograph looking NE along the fault marked by a black line on the inset map, from the point marked by the orange circle.

(∼20 m and 25 m, respectively), while the Holocene uplift at Lindos is 2.3 m and 0.2 m at Plimmiri. This discrepancy is easily explained by uplift in large, infrequent earthquakes, where only part of the fault has ruptured during the late Holocene. Smaller, more regular earthquakes would be expected to distribute uplift more evenly. Thus, although uplift over several earthquakes is a possibility, we (like Kontogianni *et al.* 2002) treat the uplift of the last 6000 yr as the result of a single large earthquake.

3.2 Magnitude of uplift

Eustatic sea level in the eastern Mediterranean over the past 6000 yr is widely agreed not to have been higher than at present (e.g. Lambeck 1995; Sivan *et al.* 2004; Lambeck & Purcell 2005) and thought to have remained stable (e.g. Lambeck & Bard 2000; Siddall *et al.* 2003), although variations at the sub-1-m level cannot be ruled out. It is therefore reasonable to assume that the elevations of the palæoshorelines represent a lower bound on coseismic up-

lift. Investigation of faults capable of producing the observed uplift distribution using dislocation modelling yields a solution with a reverse fault dipping at about 60° (Kontogianni *et al.* 2002). This steep dip is required by the absence of uplift on the western coast of Rhodes; a reverse fault that dipped more shallowly than 60°, while lifting up the east coast by more than 3 m, would also lift up the western coast.

The elevations of the palæoshorelines must, however, be interpreted with care; in the time since they were lifted up, it is probable that some of them have been disturbed by tectonic activity. A northwest-dipping normal fault, part of the Siana fault zone of ten Veen & Kleinspehn (2002), is clearly expressed in the topography of the western part of the island (Figs 4b and 3). We could not make an unequivocal measurement of rake for this fault, but its morphology (including a steeply incised gorge in its footwall) shows that it is predominantly normal in character and downthrown to the NW. The fault strikes 200°, its dip at the surface is 75°, and it can be traced for 10 km along strike to the north of the location illustrated

in the inset map in Fig. 4(c). Ten Veen and Kleinspehn mapped numerous other normal faults to the south of the locality in Fig. 3. NW-dipping normal faults have also been observed offshore from the southern tip of Rhodes (Mascle *et al.* 1986), and GPS data show 4-6 mm yr^{-1} extension between stations on Rhodes and the Datça peninsula in SW Turkey (Fig. 1; Nocquet 2012; Tiryakioğlu *et al.* 2013). We therefore consider it likely that normal faulting drops down the western coast of Rhodes, possibly removing evidence of uplift in occasional large reverse-faulting earthquakes.

Our analysis modifies the distribution of uplift used by Kontogianni *et al.* (2002). We also omit the two points marked in black in Fig. 3. The more southerly of those points (Charaki) may be affected by local normal faulting with small throw (see Figs 4a and c); at the northern point (in Rhodes Town), the cliffs are ≲2 m high, so not high enough to record a palæoshoreline at the >2.5 m elevation that would be expected from the elevation of neighbouring points. We also use a new measurement of palæoshoreline height at Stegna (3 m; Fig. 3).

The sites marked in red in Fig. 3(b) show the locations used in our analysis of uplift.

3.3 Timing of uplift

We obtained radiocarbon dates for 15 lithophagids (*L. lithophaga*), 1 arcoid and 4 corals, with dates shown in Table 1 and Fig. 5. The dating was carried out at the Oxford Radiocarbon Accelerator Unit. We calculated a local reservoir correction, ΔR, of 38 ± 86 yr (1σ) for Rhodes, using reservoir ages from around the eastern Mediterranean (Siani *et al.* 2000; Reimer & McCormac 2002; Boaretto *et al.* 2010) and the tools on www.calib.org. The dates shown in Table 1 were calculated using this value of ΔR, the IntCal13 and Marine13 curves (Reimer *et al.* 2013) and the OxCal program (Bronk Ramsey 1995).

The samples were taken from localities along the eastern coast of Rhodes (Fig. 5). Despite extensive searching, we could find few datable remains of marine organisms, possibly because the maximum shoreline elevation on Rhodes is much lower than in other places that have yielded more abundant samples (e.g. Stewart 1996; Kershaw & Guo 2001; Shaw *et al.* 2008). Except at Kallithea (red in

Fig. 5), we could find uplifted marine organisms only in limestone outcrops protected from marine erosion by wide sandy beaches. All but three of the samples gave Holocene ages. If the size of the sample was sufficiently large it was tested for diagenetic alteration using a scanning electron microscope; the three lithophagids that gave ages older than 30 000 yr were all too small to be tested for diagenetic alteration, so their ages may be unreliable. The single arcoid shell gave an age of 2000 BP; this shell was found wedged within an abandoned lithophaga boring in what was interpreted at the time of collection to be a life position.

The remaining samples fall into two age groups: one clustered around 6000 BP and another around 4000 BP (see Fig. 5). We interpret the older group as being associated with the mid-Holocene stabilization of sea level. Progradation of deltas was widespread at that time (Stanley & Warne 1994) and this group of samples could have been buried by the increased supply of sediment. We interpret the second group (which consists entirely of lithophagids) as representing organisms that died before uplift in the earthquake. Until recently, radiocarbon ages on lithophagids in tectonic settings were usually interpreted as representing the date of death of the organism. Shaw *et al.* (2010) demonstrated, however, that lithophagids associated with the uplift of shorelines in the AD 365 earthquake in western Crete gave ages that were systematically at least 350 yr older than the uplift event. Evelpidou *et al.* (2012) suggested a similar age offset for lithophagids from tsunami boulders in the Gulf of Euboea. An age offset of 400 yr would represent incorporation of about 5 per cent radioactively 'dead' carbon from the host rock (Shaw *et al.* 2010).

The ages from this second group provide an earliest possible date for the earthquake. The youngest calibrated date (sample TZAM12) is between 2009 BC and 1532 BC at the 95 per cent level of confidence. Incorporating a 400-yr offset, by analogy with the samples from western Crete (Shaw *et al.* 2008, 2010), brings that age range to ~1600–1100 BC. We have scanned the arcoid (sample TZAM20) using EDBS and determined that it is formed entirely of aragonite, so its age of 316 BC to AD 155 is likely to represent the date of death of the organism. This range therefore provides an alternative earliest possible date for the earthquake; if this is the case, however, the lithophaga ages are 2000–3000 yr older than the earthquake,
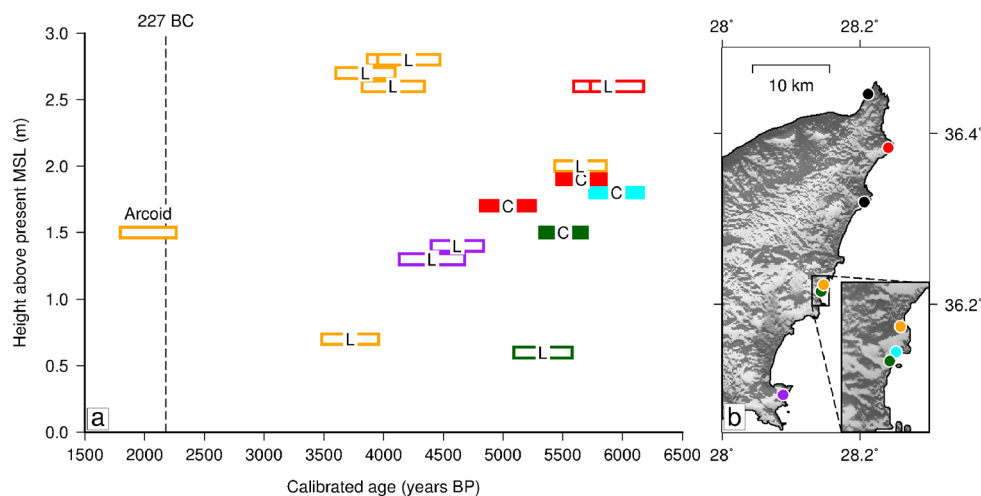

Figure 5. Ages (calibrated before 1950), heights and locations of dated samples. Rectangles in (a) show 95.7 per cent age ranges of samples. Filled rectangles (marked 'C') represent corals and empty rectangles ('marked L') represent lithophagids, except for the sample labelled arcoid. Colours correspond to the locations of samples on the map in (b). The samples that gave ages older than 30 000 yr are marked in black in (b) (Ladikou is the southern point and Rhodes Town is the northern point). The line marked '227 BC' shows the approximate date for the earthquake thought to have caused the collapse of the Colossus of Rhodes, some time between 229 and 225 BC (Ambraseys 2009).

Table 1. Details of radiocarbon dates from marine fauna found in the uplifted cliffs of Rhodes. Height is elevation (in m) above the present-day sea level. Organism gives species for lithophagids (all *L. lithophaga*), family for corals (all *Caryophyllidae*) and order for the arcoid (*Arcoida*).

Lab code	Sample ID	Height (m)	Organism	^{14}C age (years BP)	68.2 per cent probability	95.7 per cent probability
29555	AHKAL1	1.7	*Caryophyllidae*	4782 ± 31	3175 BC to 2903 BC	3320 BC to 2861 BC
30043	AHKAL3	1.9	*Caryophyllidae*	5305 ± 32	3792 BC to 3587 BC	3913 BC to 3497 BC
30044	AHKAL5A	2.6	*L. lithophaga*	5535 ± 31	4026 BC to 3801 BC	4160 BC to 3701 BC
30045	AHKAL5B	2.6	*L. lithophaga*	5453 ± 30	3941 BC to 3739 BC	4023 BC to 3639 BC
30046	AHKAL6	2.6	*L. lithophaga*	5596 ± 31	4141 BC to 3907 BC	4226 BC to 3780 BC
30049	AHLAD2A	1.7	*L. lithophaga*	34260 ± 350	36781 BC to 35826 BC	37135 BC to 35061 BC
30047	AHLIN3	1.3	*L. lithophaga*	4317 ± 27	2566 BC to 2309 BC	2727 BC to 2179 BC
30048	AHLIN6	1.4	*L. lithophaga*	4486 ± 28	2822 BC to 2572 BC	2885 BC to 2448 BC
30050	AHRT1	2.4	*L. lithophaga*	37370 ± 250	39811 BC to 39346 BC	40030 BC to 39071 BC
30051	AHRT2	2.4	*L. lithophaga*	32230 ± 160	33992 BC to 33517 BC	34189 BC to 33272 BC
28100	ARHA4	1.8	*Caryophyllidae*	5591 ± 31	4137 BC to 3901 BC	4224 BC to 3776 BC
28099	STEG10	0.6	*L. lithophaga*	5057 ± 29	3531 BC to 3320 BC	3628 BC to 3139 BC
28115	STEGSO13D	1.5	*Caryophyllidae*	5202 ± 31	3678 BC to 3481 BC	3756 BC to 3356 BC
27148	TZAM1	2.8	*L. lithophaga*	4107 ± 33	2287 BC to 2017 BC	2427 BC to 1911 BC
27214	TZAM2	2.8	*L. lithophaga*	4185 ± 31	2401 BC to 2141 BC	2521 BC to 2000 BC
27149	TZAM3	2.6	*L. lithophaga*	4073 ± 31	2240 BC to 1973 BC	2391 BC to 1869 BC
27150	TZAM4	2.7	*L. lithophaga*	3918 ± 29	2018 BC to 1765 BC	2146 BC to 1650 BC
28097	TZAM12	0.7	*L. lithophaga*	3819 ± 28	1887 BC to 1652 BC	2009 BC to 1532 BC
28115	TZAM18	2.0	*L. lithophaga*	5291 ± 32	3775 BC to 3567 BC	3912 BC to 3482 BC
28098	TZAM20	1.5	*Arcoida*	2407 ± 25	161 BC to AD 66	316 BC to AD 155

Table 2. Limits of parameter space searched systematically by our grid search, and the intervals between grid search points. The distances SW and SE from Lindos refer to the distance of the SW end of the fault from the point (28.1°E, 36.05°N) parallel to and perpendicular to a line trending 205° (the strike of the 2000 m bathymetric contour and the approximate strike of the coast). 'Bottom' refers to the depth of the lower vertical limit of rupture. All models rupture to the surface. Slip is estimated using standard least-squares methods.

	Distance SW from Lindos (parallel to coast; km)	Distance SE from Lindos (perpendicular to coast; km)	Strike (°)	Length (km)	Dip (°)	Rake (°)	Bottom (km)
Upper limit	30	30	285	90	65	90	40
Lower limit	−30	0	195	40	10	0	10
Interval	5	5	5	5	5	5	5

which is very different from the case of western Crete, where only 1 out of 15 lithophaga dates was more than 2000 yr before the earthquake. Stiros & Blackman (2013) use the presence of Hellenistic slipways at 3 m above present MSL in Rhodes town to infer that uplift occurred since the third century BC, perhaps in the c. 227 BC Rhodes earthquake (which destroyed the Colossus of Rhodes; e.g. Ambraseys 2009), but since neither the top nor the bottom of the slipways was found, the exact magnitude of any uplift is not well constrained.

We conclude that the earthquake almost certainly occurred after 2000 BC, and possibly after 300 BC.

4 FAULT PARAMETERS FROM ELASTIC MODELLING OF UPLIFT

We treat the earthquake as uniform slip on a buried rectangular fault in an elastic half-space (Okada 1985). This source is defined by nine parameters: the horizontal coordinates of the two end points of the projection of the rectangle to the surface; the depths of the upper and lower limits of rupture; the fault dip and the strike-parallel and dip-parallel components of slip. We employ a grid search to find the minimum misfit in the parameter space defined in Table 2. The problem is linear in the two components of slip, which can be obtained by standard least-squares methods if the other seven parameters are specified. However, because the observations of uplift on Rhodes are distributed close to a line parallel to the coast, it is not possible to constrain both components of slip from the

observations; we prefer to specify either the rake or the horizontal azimuth of slip vector. This allows us to investigate plausible fault orientations consistent with the regional kinematics (Section 4.3) and to avoid solutions with a right-lateral component of slip in what GPS and earthquake data show is a region of overall left-lateral shear (e.g. Shaw & Jackson 2010; Tiryakioğlu *et al.* 2013).

4.1 Constraints on acceptable fault models informed by tectonic considerations

We consider only NW-dipping faults with a reverse component of slip because this matches the dip of the subducting slab and the dips of active reverse faults in the Rhodes Basin (Woodside *et al.* 2000; Hall *et al.* 2009). We constrain the dip of the fault to be less than 65° because this is the maximum dip reliably observed for reverse-faulting earthquakes (e.g. Sibson & Xie 1998; Middleton & Copley 2013). Slip appears to have reached the surface in many of the large reverse-faulting earthquakes of recent years (e.g. Avouac *et al.* 2006; Chlieh *et al.* 2007; Liu-Zeng *et al.* 2009; Lay *et al.* 2011; Ozawa *et al.* 2011; Vigny *et al.* 2011), and there is evidence that where it does not, post-seismic afterslip (the effects of which are included in the observed heights of the palæoshorelines and therefore our estimates of earthquake source parameters) often extends to the surface (e.g. Hsu *et al.* 2006; Mahsas *et al.* 2008; Copley 2014). An earthquake of the size required to produce several metres of uplift on Rhodes may therefore be expected to rupture the seafloor, or at least be associated with a visible bathymetric feature where

the fault projects to the surface. We therefore set the upper surface for all our models to be at zero depth. Reverse faults that offset Quaternary sediments are observed in the Rhodes Basin (Hall *et al.* 2009), suggesting that this restriction is reasonable.

The likely maximum depth for the lower vertical limit of rupture is given by the thickness of the seismogenic layer underneath Rhodes. Microseismicity reaches a depth of about 40 km on Crete (Meier *et al.* 2004), and the seismogenic thickness is similar in many other subduction zones (Tichelaar & Ruff 1993), so we allow the depth of the bottom of the rupture in our fault models to be 40 km or shallower.

We specify fault position by the location of one end of the surface projection of the fault, with the other end defined by strike and length. The position of the SW end of the fault in the direction parallel to the coast is well defined by the sharp drop in observed palæoshoreline height SW of Lindos (Fig. 3b). We assume (as do Kontogianni *et al.* 2002) that the steep bathymetric escarpment between Rhodes and the Rhodes Basin is maintained through active faulting, an assumption supported by the >200 m elevations of Quaternary marine terraces on Rhodes (Gauthier 1979; Kontogianni *et al.* 2002). Thus the surface projection of the fault is assumed to be NW of the base of the escarpment, which is ∼30 km from the coast. The location of the NE end of the surface projection is constrained only by the absence of observations of either uplift or active reverse faults in the part of the Turkish coast NE of Rhodes, so it is reasonable to assume that the fault does not extend that far; we therefore limit its length to ≤80 km.

The only constraint on the strike of the fault is the existence of the steep bathymetric escarpment SE of Rhodes. If, as seems probable, this escarpment is maintained through repeated faulting, a strike parallel to the contours of bathymetry would be expected. However, the contours of bathymetry ($205+5/-1°$) are subparallel to the GPS velocities of Rhodes relative to Nubia (∼195°). So if the horizontal azimuth of slip was to match the direction of the GPS velocity, either very oblique slip on a fault striking 205° or a fault that strikes more E–W than the contours of bathymetry is required. Fault models with strike 205° and oblique slip do not match the observed uplift distribution, so we consider two sets of possible fault models that can fit the observed uplift (discussed in Section 4.3):

(1) Pure reverse faults that strike parallel to the contours of bathymetry. For this set of models, it is necessary to infer additional faulting somewhere to account for the missing component in the overall convergence between Rhodes and Nubia. For these models, rake is fixed at 90°.

(2) Faults with the horizontal azimuth of slip fixed to 195° (the direction of the relative motion), and strike allowed to vary between 205° and 285°.

4.2 Range of acceptable solutions and trade-offs between parameters

We set 40 cm as an upper limit for an acceptable misfit because, while individual uplift measurements may not be accurate to better than 40 cm (Fig. 6), the overall RMS misfit is dominated by the misfit at the sites where uplift is greatest; these individual misfits can be of the order of a metre for an overall RMS misfit of 40 cm (see supplementary material for further details). Some parts of parameter space are excluded by the distribution of observed uplift. No fault model with a dip less than 20° or with a lower limit of rupture shallower than 20 km fits the observed uplift to better than 40 cm RMS misfit. Similarly, unacceptable misfits are found if the location

of the SW end of the fault is further than 5 km from Lindos in the direction parallel to the coast.

A wide variety of tectonically plausible fault models fit the observed uplift satisfactorily. We illustrate this range of solutions in Fig. 6 and Table 3; in Figure 6 they are arranged in two groups: pure reverse faulting on faults parallel to the contours of bathymetry in columns 1 (20–25 km rupture depth) and 2 (40 km rupture depth) and slip in the direction of southern Aegean–Nubia relative motion on faults that are oblique to the contours of bathymetry (column 3). In all cases, trade-offs arise because the observations of uplift are confined to an almost linear piece of coastline (see supplementary material for further information). Solutions B and C (Fig. 6) illustrate the trade-off between dip and magnitude of slip in the pure reverse-faulting case, which arises because the steeper the dip of the fault, the more sharply uplift drops off with distance from the fault. Models D and E illustrate a trade-off between magnitude of slip and distance of the fault from the coast, for similar reasons. A third trade-off exists between the depth extent of faulting and the distance from the coast: fault models that rupture to 40 km depth are able to fit the observed uplift with surface projections up to 25–30 km from the coast (E, F), whereas for fault models rupturing from the surface to 20 km depth the maximum distance from the coast is 10 km (A, C). There is also a trade-off between fault length and magnitude of slip, but this is relatively small, contributing a variation of about 1 m in slip. Faults with lengths between 45 and 75 km (models A and F) are able to fit the observed uplift equally well, but we consider that longer faults are marginally more likely because their ratio of slip to length is more typical of continental earthquakes (Scholz *et al.* 1986; Wells & Coppersmith 1994).

Similar trade-offs apply to fault models with oblique slip (models G–I), but their effects are harder to discern because of variation in strike between models. It should be noted that some of the fault models in Fig. 6 predict ∼1 m uplift on the Datça Peninsula in SW Turkey (Fig. 1). While this has not been observed, there have been few detailed studies of the region, and some of the shorelines are subject to subsidence related to the N–S extension of SW Turkey (e.g. Altunel *et al.* 2003; Uluğ *et al.* 2005). Furthermore, uplift scales linearly with slip, so that far-field uplift is much more sensitive to uncertainties in sea level history. For example, the combination of a 25 per cent increase in magnitude of slip and a 1 m eustatic sea-level rise following uplift could conceal 1 m of far-field uplift while keeping observed heights of the highest palæoshorelines on Rhodes the same relative to modern sea level.

This uncertainty in sea level also means that it would be unproductive to analyse the possible effects of interseismic deformation and post-seismic viscous relaxation, since our estimates of palæoshoreline uplift are already minima (Section 3). For the fault geometries in Fig. 6, the sites where uplift was observed on the coast are in the region where interseismic motion might be expected to cause subsidence (e.g. Sieh *et al.* 1999; Ader *et al.* 2012). Moreover, modelling of post-seismic viscous relaxation for a fault in a similar setting on SW Crete suggests that apart from in the region beyond the lower (down-dip) limit of faulting (which in the present case is underwater), its contribution is minimal (<10 per cent of observed palæoshoreline height; Shaw *et al.* 2008).

4.3 Fault models consistent with uplift and bathymetry

We have investigated two cases; in one the fault responsible for uplift slips predominantly in the reverse sense, in the other the slip
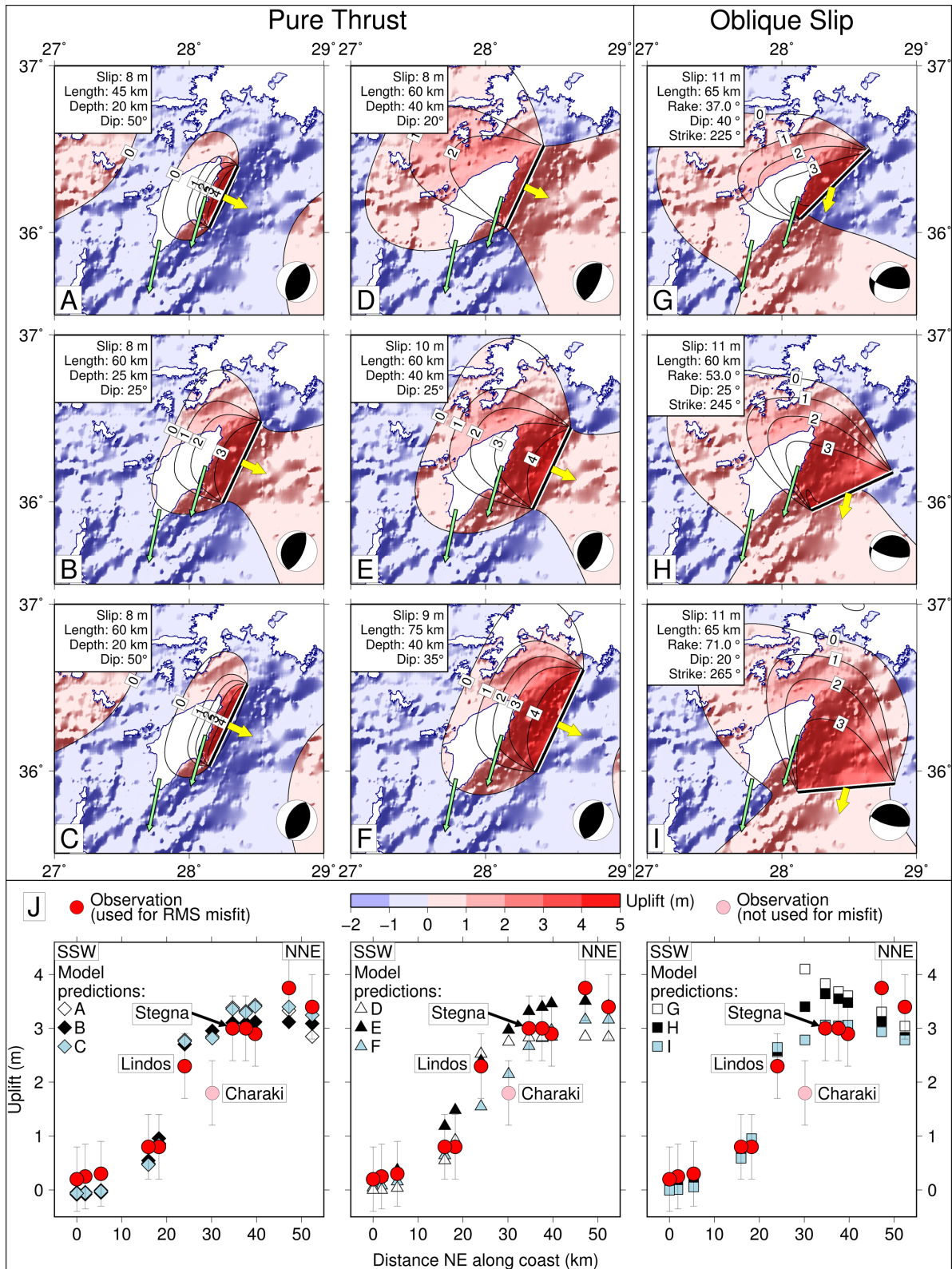
Figure 6. Predicted uplift distributions for fault models matching the observed uplift on Rhodes and their source parameters, which are also listed in Table 3. A–F are pure reverse-faulting solutions with their strike constrained to be parallel to the bathymetric contours (205°), and models G–I are oblique-slip models with no constraint on strike but a horizontal azimuth of slip vector constrained to be parallel to the GPS velocity at Archangelos relative to Nubia (the northern green arrow; DeMets *et al.* 2010; Nocquet 2012). J compares predicted uplift for the labelled models to observed uplift (shown in red) at the sites in Fig. 3, with ±60 cm error bars to illustrate the possible effects of errors in measurement of palæoshoreline height and estimation of the present-day sea level. Distance NE refers to the distance in the 025° direction from the southernmost of the uplift sites shown in Fig. 3. Depth refers to the lower limit of rupture in the model, as all fault models rupture from the surface to this depth.

Table 3. Source parameters for earthquake source models in Fig. 6. SW end (E) and SW end (N) refer to the longitudinal and latitudinal coordinates respectively of the southwest end of the fault surface projection. AD 365 refers to the preferred earthquake model of Shaw *et al.* (2008) for the AD 365 earthquake that uplifted SW Crete, used in this study to compare modelled tsunami heights (Section 5). M_W was calculated using the formula of Hanks & Kanamori (1979) and an elastic modulus for the upper crust of 3×10^{10} Nm.

Source	SW end (E,°)	SW end (N,°)	Strike (°)	Length (km)	Top (km)	Bottom (km)	Dip (°)	Rake (°)	Slip (m)	RMS Misfit (cm)	M_w
A	28.15	36.031	205	45	0	20	50	90	8	25	7.7
B	28.251	35.993	205	60	0	25	25	90	8	25	7.7
C	28.15	36.031	205	60	0	20	50	90	8	25	7.8
D	28.15	36.031	205	60	0	40	20	90	8	25	7.9
E	28.352	35.955	205	60	0	40	25	90	10	23	7.9
F	28.375	35.996	205	75	0	40	35	90	9	26	8.0
G	28.139	36.082	225	65	0	40	40	37	11	29	8.0
H	28.221	35.947	245	60	0	40	25	53	11	29	8.0
I	28.119	35.871	265	65	0	40	20	71	11	29	8.0
AD 365	23.8	34.9	315	100	0	45	30	90	20	N/A	8.5

is highly oblique, matching the direction of relative motion between Rhodes and Nubia. Models A–F (Fig. 6) represent the former case and models G–I the latter. Large-magnitude earthquakes with slip as oblique as model G are rare but have been observed, for example in the 2009 Dusky Sound earthquake (Beavan *et al.* 2010), while less oblique slip vectors such as that of model I are more common (e.g. Avouac *et al.* 2006; Liu-Zeng *et al.* 2009). However, although fault models G–I are able to fit the uplift data with a low misfit, there are several features of their uplift distributions that make a coast-parallel reverse fault more likely.

Oblique slip on faults close to the coast (models G–H) predicts a maximum in uplift immediately NE of Lindos, which is not observed (see spatially organized misfits in Fig. 6j), so for models G and H local normal faulting and subsidence must be inferred in order to explain the observed uplift distribution. Kontogianni *et al.* (2002) indeed suggest that subsidence from a normal fault is necessary to explain the lower palæoshoreline height at Charaki (pink in Fig. 6j) relative to Lindos, further SW. Models G and H require subsidence of ~2 m at Charaki in order to fit the observations, as well as smaller amounts of subsidence (~0.5 m) further north. We suggest that the most likely set of faults to have caused subsidence at Charaki are the obvious W-dipping faults in the massif 2–3 km north of Charaki (Gauthier 1979; Fig. 4, this study). Charaki is in the hanging wall of these faults while Stegna is in their footwall, and the 1.2 m difference in palæoshoreline height over the 6 km between the two sites is most easily explained by slip on these faults, especially as there is no obvious N-dipping normal fault between Charaki and Lindos to the SW. However, in order to counter the modelled uplift from faults G and H in Fig. 6, both Charaki and Stegna must subside in presumed normal faulting for which there is no evidence. We therefore discount both models G and H.

The observed coastal uplift cannot be used to differentiate between the more E–W fault in model I and the reverse-faulting models A–F, as their predicted uplift distributions are almost indistinguishable over the region where data are available. However, model I does predict maximum uplift in the deepest part of the Rhodes Basin, with no recognizable bathymetric relief associated with the projection of the fault to the surface. This makes faulting similar to that in model I an implausible way to explain the longer-term Quaternary uplift on Rhodes, and since the location of the maximum elevation of the marine terraces and the maximum late Holocene palæoshoreline uplift approximately coincide (Kontogianni *et al.* 2002), we suggest that the long-

term and short-term uplift probably result from slip on the same fault. We therefore discount faulting with the more E–W strike of model I.

From the range of parameter space we investigated (illustrated in Figs 6a–f), we conclude that such a fault is likely to have a length of 45–75 km, a dip of 20–60°, a strike of 205°, slip of 8–11 m and a lower limit of rupture between 20 and 40 km depth. The resultant earthquake would have had a magnitude $M_W \geq 7.7$, which clearly represents a significant regional hazard.

5 TSUNAMIGENIC POTENTIAL OF AN EARTHQUAKE UPLIFTING RHODES

The Hellenic Trench System earthquakes of AD 365 and AD 1303 both caused tsunamis that damaged coasts around the eastern Mediterranean, including the Nile Delta. Our radiocarbon data (Section 3.3) suggest that the earthquake responsible for uplift on Rhodes occurred long before either of these tsunamis, but a reverse-faulting earthquake of $M_W \geq 7.7$ might be expected to cause at least a locally damaging tsunami. We therefore model tsunamis from fault models A–F (Fig. 6), using the calculated seafloor uplift distribution as an initial perturbation in sea surface height. Uncertainties in our tsunami initial condition and the lack of readily available high-resolution bathymetry for eastern Mediterranean coasts mean that we restrict our models to the offshore region (>20 m depth), using MOST (Titov & Synolakis 1995, 1998) to model propagation on a 1′ ETOPO bathymetric grid (Amante & Eakins 2009).

Tsunami propagation is approximately radial (Fig. 7a). Traveltimes are approximately the same for all models: ~40 min to Cyprus and ~60 min to the Nile Delta. Some fault models (notably E–F) predict higher tsunami heights over a wider area than others (fault model D predicts the smallest tsunami). Maximum tsunami heights are illustrated in Fig. 7(b), showing predicted heights of >1 m offshore from Rhodes and SW Turkey, and also off the coast of Cyprus for the sources with greater tsunamigenic potential (Model E). These wave heights would be expected to translate into higher runup heights on land; for example, the 2010 Mentawai earthquake (M_W 7.8) produced a maximum wave height of <1 m in the open ocean but 6 m runup on land (Hill *et al.* 2012).

The shallow bathymetry offshore and the associated non-linear effects of bottom friction and wave breaking on dissipation of
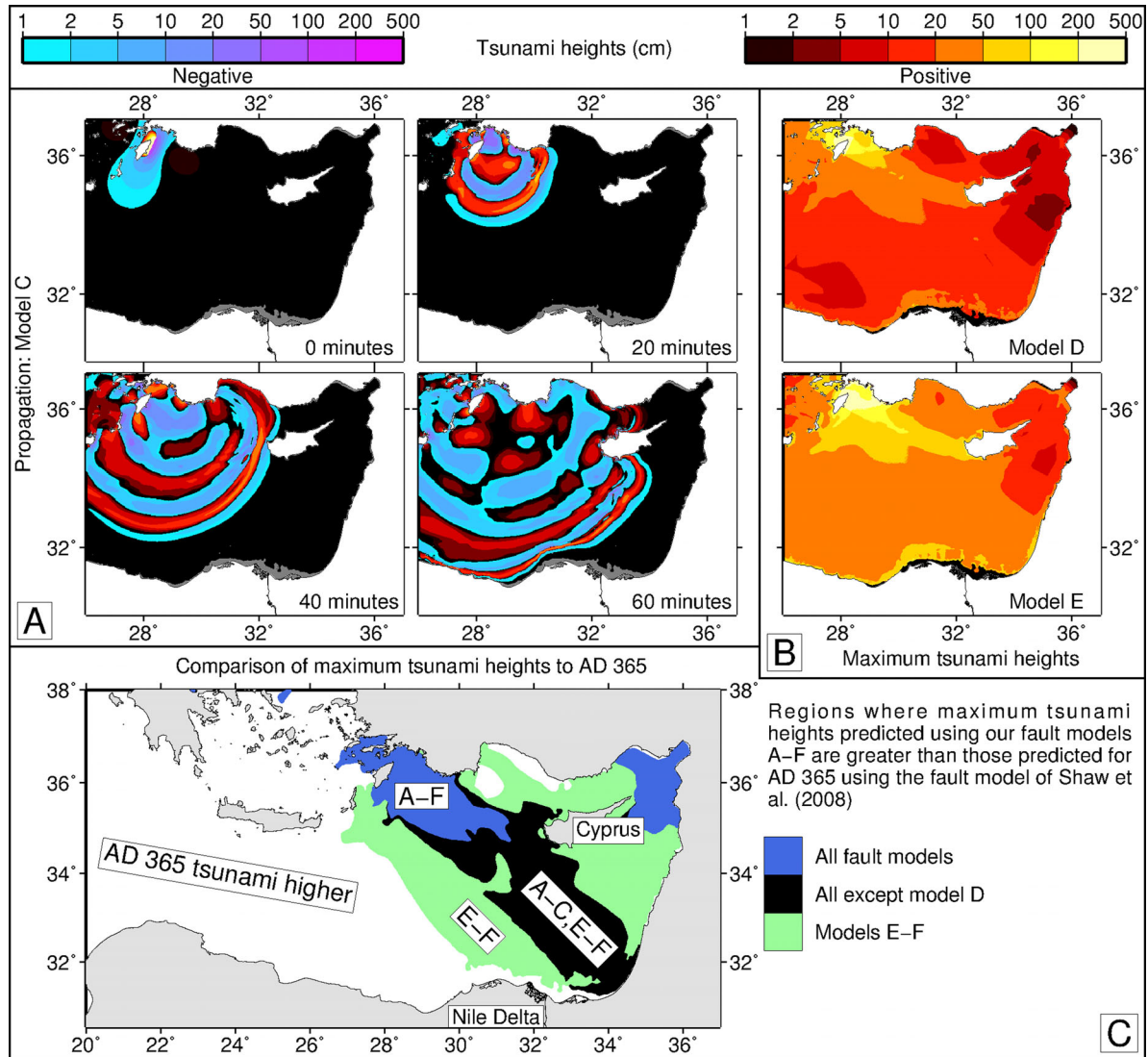
Figure 7. Modelled tsunamis using some of the fault models in Fig. 6 as initial conditions. Panel (a) shows wave propagation across the eastern Mediterranean at 20, 40 and 60 min after the earthquake, using fault model C as an initial condition. Panel (b) shows maximum predicted wave heights for fault models D and E. Panel (c) shows the regions where predicted maximum wave heights resulting from the labelled fault models (from Fig. 6) are higher than those predicted using the best-fitting uplift model for AD 365 (Shaw *et al.* 2008) as an initial condition. The source parameters for the AD 365 fault model are shown in Table 3.

tsunami energy make it difficult to estimate how offshore tsunami heights might relate to onshore flooding (Korycansky & Lynett 2005; ten Brink *et al.* 2007). For this reason, we compare the predicted tsunami heights using our fault models with those predicted for AD 365 using the preferred fault model of Shaw *et al.* (2008) (Fig. 7c). We assume that since there is abundant historical evidence for damage throughout the Nile Delta in AD 365 (Shaw *et al.* 2008; Ambraseys 2009), a tsunami model where offshore wave heights are greater than those predicted for AD 365 is likely to be capable of damage onshore. Most of our fault models predict tsunami heights smaller than for AD 365 off the Nile Delta, but tsunamis predicted from models E–F predict higher wave heights off the eastern Nile Delta.

We therefore conclude that of the plausible fault models investigated, even those with the lowest tsunamigenic potential would be capable of significant regional tsunami damage in SW Turkey and Rhodes, while those with the highest tsunamigenic potential (from higher-magnitude fault models) would also be capable of damage to Cyprus and the Nile Delta.

6 TECTONIC IMPLICATIONS

6.1 Accommodation of transcurrent motion between Nubia and the Aegean

We have argued in Section 4.3 that the uplift of Rhodes probably arises from almost pure reverse slip on a fault that crops out at one of the steep bathymetric features of its eastern coast. This raises the question of where the remainder of the highly oblique relative motion between Nubia and the southern Aegean is accommodated. It is commonly observed that oblique convergence at plate boundaries is split between parallel reverse and strike-slip faults with orthogonal slip vectors (an arrangement often referred to as 'partitioning', e.g. Fitch 1972; McCaffrey 1996; Lay *et al.* 2013). Where such a configuration is observed, the strike-slip fault invariably lies in the overriding plate. The relative motions of the GPS sites on Rhodes, both with respect to Nubia and with respect to the interior of the Aegean, rule out the accommodation of the transcurrent motion on a fault that lies to the north and west of those sites, which are in the eastern part of Rhodes. Therefore, if this configuration of faulting
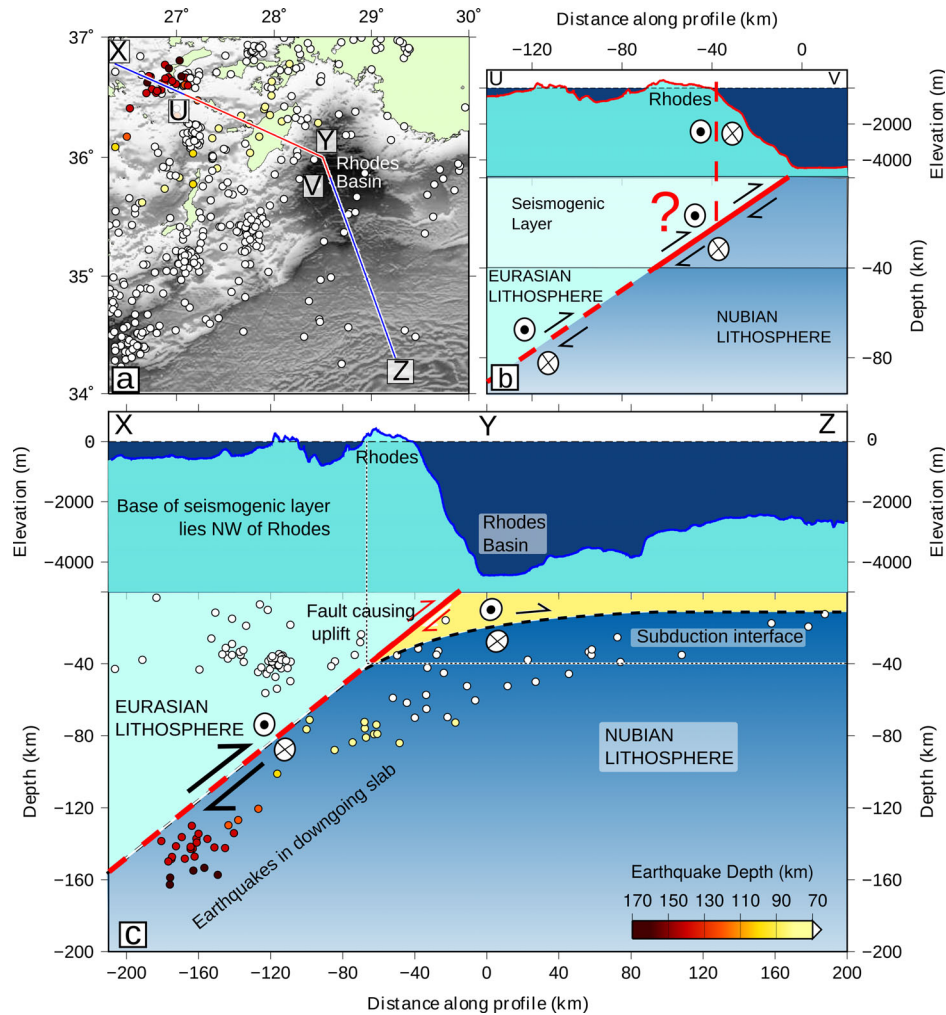
Figure 8. Possible configurations of faulting around the Rhodes Basin. Panel (a) shows bathymetry (SRTM30+; Becker *et al.* 2009), the locations of earthquakes from the EHB catalogue (Engdahl *et al.* 1998) and the paths of the profiles in (b) and (c). Panel (b) shows a possible interpretation of faulting where the floor of the Rhodes Basin is part of stable Nubia, and the strike-slip component of Rhodes–Nubia convergence is accommodated on a fault (or shear zone) between the reverse fault and the coast. Topography is a vertically exaggerated profile along the red line UV in (a). Panel (c) shows our preferred interpretation in which Rhodes is uplifted on a steeper-dipping fault above the main subduction interface. The earthquakes in this figure are projected onto the blue line XYZ in (a) from 40 km either side. The blue line shows a vertically exaggerated topographic profile along the line XYZ in (a).

applies, any strike-slip motion must occur in the <30 km between the outcrop of the reverse fault and the coast of Rhodes and, as illustrated in Fig. 8(b), the strike-slip and reverse faults must intersect at about 20 km as has, for example, been suggested for Haida Gwaii (Lay *et al.* 2013).

There is, however, little evidence to support the configuration of faulting illustrated in Fig. 8(b). In particular, no earthquake within the overriding plate of this region has exhibited a strike-slip focal mechanism. Furthermore, over the last 6000 yr, the earthquake responsible for uplift of Rhodes only accounts for ∼10 m of the 40 m shortening in the direction perpendicular to the coast expected from GPS data (bearing 115°), which suggests that at least one additional fault with a reverse component of motion is required to accommodate the remainder of the Rhodes–Nubia convergence. An alternative solution, illustrated in Fig. 8(c), is suggested by the observation that the subduction interface is essentially aseismic, and by the suggestion of Shaw *et al.* (2008) that the rare great earthquakes in the Hellenic plate boundary zone take place on reverse faults within the overriding continental crust. For western Crete, where the relative motion is perpendicular to the strike of the plate

boundary, Shaw *et al.* (2008) suggested that the compressional deviatoric stresses causing this reverse faulting arise from a reduction in the slip velocity from the deeper to the shallower parts of the subduction interface (Shaw *et al.* 2008, fig. 5). We extend this idea to the eastern end of the plate boundary zone, suggesting that the subduction interface absorbs, predominantly aseismically, most of the oblique convergence between Nubia and the Aegean, but with some or all of the convergence being taken up on arc-perpendicular reverse faults (Fig. 8c).

6.2 Accommodation of motion near the Pliny and Strabo Trenches

The Pliny and Strabo Trenches, to the SW of Rhodes, are much further from the nearest land than either the Rhodes Basin or the Hellenic Trench, so faulting in the area would not be expected to produce coastal uplift. However, there have been numerous small earthquakes in this region since 1960, which provide an insight into its kinematics. Fig. 9 shows focal mechanisms for earthquakes
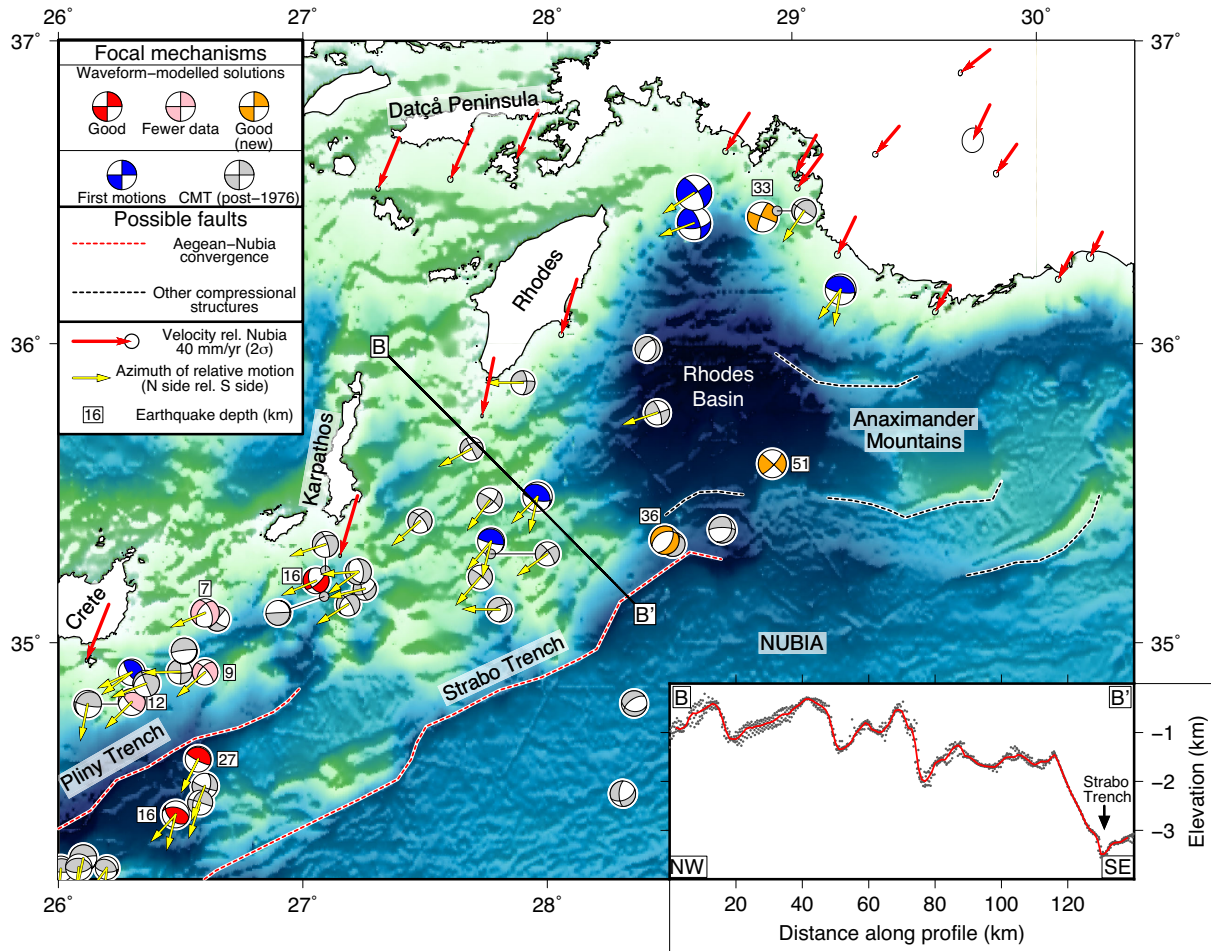
Figure 9. Earthquake focal mechanisms and slip vectors for the Pliny and Strabo Trenches and the Rhodes Basin. Focal mechanisms appearing in red, pink and orange are waveform-modelled, and are sourced either from the compilation of Shaw & Jackson (2010) (red and pink) or from this study (orange). The numbers next to focal mechanisms show earthquake depths (in km). For the strike-slip and oblique earthquakes, the slip vectors chosen are the ones that are consistent with left-lateral shear and slip vectors in the range 180–280°. For dip-slip earthquakes, slip vectors are shown where the motion of a plausible hanging wall relative to a corresponding footwall is in this range of azimuths. Earthquakes that do not fit this pattern are shown without slip vectors. GPS velocities are from Nocquet (2012) and have been rotated so that they are relative to Nubia using the pole of DeMets *et al.* (2010). Waveform modelling used the MT5 version (Zwick *et al.* 1994) of the inversion algorithm of McCaffrey & Abers (1988) and McCaffrey *et al.* (1991).

whose depths are either unknown (from the CMT catalogue or first motions; McKenzie 1972, 1978; Dziewonski *et al.* 1981; Ekström *et al.* 2012) or determined by waveform modelling to be in the overriding Aegean lithosphere (Shaw & Jackson 2010, this study).

GPS velocities on the Dodecanese islands (Rhodes and Karpathos) show that motion of the islands relative to Nubia is oblique (∼45°) to both the subduction zone and the Pliny and Strabo Trenches. However, the slip vectors of the strike-slip and oblique-normal earthquakes in Fig. 9 are mostly trench-parallel and compatible with left-lateral shear, although some of this faulting may be related to arc-parallel extension. Our interpretation of this pattern of slip vectors, which also explains the ∼1800 m of relief across the Strabo Trench at its northern end, is that the trench-parallel component of Aegean–Nubia convergence is accommodated through distributed strike-slip faulting while the trench-perpendicular (shortening) component is taken up on large reverse faults, similar to those responsible for uplift of Crete and Rhodes.

This form of partitioning is similar in geometry and scale to that suggested for Haida Gwaii, in the Cascadia subduction zone (Lay *et al.* 2013; Szeliga 2013), where a large, reverse-faulting earthquake occurred in October 2012. The interpretation that the Pliny and Strabo Trenches are the expressions of reverse faulting also provides a possible source location for the AD 1303 earthquake, which historical data suggest occurred in the Hellenic Arc, somewhere between Crete and Rhodes (Ambraseys 2009; Yolsal-Çevikbilen & Taymaz 2012). Our radiocarbon data show that this earthquake was not the one responsible for the observed uplift of Rhodes, so the AD 1303 source probably lies SW of Rhodes.

6.3 Implications for arc-perpendicular normal faulting

While arc-parallel and arc-perpendicular normal faults are equally prominent in the geomorphology of the Hellenic plate boundary zone (e.g. Armijo *et al.* 1992; ten Veen & Kleinspehn 2002; Caputo *et al.* 2010; Gallen *et al.* 2014), the focal mechanisms that have been obtained for normal-faulting earthquakes in the past 60 yr show faulting only on the arc-perpendicular normal faults (i.e. arc-parallel extension). Furthermore, the present-day strain-rates derived from GPS observations (e.g. Floyd *et al.* 2010; Reilinger *et al.* 2010; Nocquet 2012) show arc-parallel extension and predominantly arc-perpendicular contraction (England *et al.* 2015, their fig. 1b). We

suggest that arc-perpendicular extension is suppressed by the compressional deviatoric stresses discussed in Section 6.1 and that extension occurs only in association with the release of compressional stress when the rare great earthquakes occur, as observed by Farías *et al.* (2011) after the 2010 M_W 8.8 Maule earthquake and by Asano *et al.* (2011) after the 2011 Tohoku-oki earthquake.

7 CONCLUSIONS

Elevated marine palæoshorelines on Rhodes provide evidence for late-Holocene tectonic uplift, and the presence of higher marine terraces shows that uplift has been continuous throughout the Quaternary. The morphology of the raised Holocene shorelines, their relationship to terrace elevations and new AMS radiocarbon dates from uplifted marine fauna are most consistent with uplift in a single earthquake after 2000 BC. Widespread normal faulting in the centre of Rhodes means that several source parameters (notably the dip) are poorly constrained, but the earthquake appears to have been a large reverse-faulting event, probably on a steeper-dipping fault above the main subduction interface. If, as seems likely, the same fault is responsible for the late-Holocene and Quaternary uplift, it cannot also accommodate the left-lateral shear observed between Rhodes and Nubia. We suggest that, instead, this NE–SW component is accommodated by oblique slip on a lower subduction interface beneath the Rhodes Basin, although strike-slip faulting further out into the basin is also possible. In the region of the Pliny and Strabo Trenches (SW of Rhodes), earthquakes occur shorewards of the trenches but with trench-parallel slip vectors. This suggests that the Pliny and Strabo trench system may be partitioned in a similar manner to Haida Gwaii, in the Cascadia subduction zone, and that the relief across them may be an expression of reverse faulting; a fault outcropping in either the Pliny or Strabo Trench is a possible location for the AD 1303 earthquake. Modelling of tsunami propagation from a range of tectonically plausible earthquake sources suggests that earthquakes on the fault uplifting Rhodes represent a significant tsunami hazard for Rhodes and SW Turkey, and also possibly for Cyprus and the Nile Delta, but uncertainties in earthquake source parameters prevent a more accurate assessment of tsunami hazard.

REFERENCES

Ader, T. *et al.*, 2012. Convergence rate across the Nepal Himalaya and interseismic coupling on the Main Himalayan Thrust: implications for seismic hazard, *J. geophys. Res.,* **117**(B4), B04403, doi:10.1029/2011JB009071.

Aksu, A., Hall, J. & Yaltırak, C., 2009. Miocene–Recent evolution of Anaximander Mountains and Finike Basin at the junction of Hellenic and Cyprus Arcs, eastern Mediterranean, *Mar. Geol.,* **258**(1–4), 24–47.

Aksu, A., Hall, J., Yaltırak, C., Çınar, E., Küçük, M. & Çifçi, G., 2014. Late Miocene–Recent evolution of the Finike Basin and its linkages with the Beydağlari complex and the Anaximander Mountains, eastern Mediterranean, *Tectonophysics,* **635,** 59–79.

Altunel, E., Stewart, I., Barka, A. & Piccardi, L., 2003. Earthquake Faulting at Ancient Cnidus, SW Turkey., *Turkish J. Earth Sci.,* **12**(1), 137–151.

Amante, C. & Eakins, B.W., 2009. *ETOPO1 1 arc-minute global relief model: procedures, data sources and analysis*, US Department of Commerce, National Oceanic and Atmospheric Administration, National Environmental Satellite, Data, and Information Service, National Geophysical Data Center, Marine Geology and Geophysics Division.

Ambraseys, N. & Synolakis, C., 2010. Tsunami Catalogs for the Eastern Mediterranean, revisited, *J. Earthq. Eng.,* **14**(3), 309–330.

Ambraseys, N.N., 2009. *Earthquakes in the Mediterranean and Middle East: A Multidisciplinary Study of Seismicity up to 1900,* Cambridge Univ. Press.

Armijo, R., Lyon-Caen, H. & Papanastassiou, D., 1992. East-west extension and Holocene normal-fault scarps in the Hellenic arc, *Geology,* **20,** 491–494.

Asano, Y., Saito, T., Ito, Y. & Shiomi, K., 2011. Spatial distribution and focal mechanisms of aftershocks of the 2011 off the Pacific coast of Tohoku Earthquake, *Earth Planets Space,* **63,** 669–673.

Avouac, J.-P., Ayoub, F., Leprince, S., Konca, O. & Helmberger, D.V., 2006. The 2005, Mw 7.6 Kashmir earthquake: sub-pixel correlation of ASTER images and seismic waveforms analysis, *Earth Planet. Sci. Lett.,* **249,** 514–528.

Beavan, J., Samsonov, S., Denys, P., Sutherland, R., Palmer, N. & Denham, M., 2010. Oblique slip on the Puysegur subduction interface in the 2009 July Mw 7.8 Dusky Sound earthquake from GPS and InSAR observations: implications for the tectonics of southwestern New Zealand, *Geophys. J. Int.,* **183**(3), 1265–1286.

Becker, J.J. *et al.*, 2009. Global Bathymetry and Elevation Data at 30 Arc Seconds Resolution: SRTM30_PLUS, *Mar. Geod.,* **32**(4), 355–371.

Boaretto, E., Mienis, H. & Sivan, D., 2010. Reservoir age based on pre-bomb shells from the intertidal zone along the coast of Israel, *Nucl. Instrum. Methods Phys. Res. B,* **268**(7–8), 966–968.

Boulton, S. & Stewart, I., 2015. Holocene coastal notches in the Mediterranean region: Indicators of palaeoseismic clustering? *Geomorphology,* **237,** 29–37.

Bronk Ramsey, C., 1995. Radiocarbon calibration and analysis of stratigraphy; the OxCal program, *Radiocarbon,* **37**(2), 425–430.

Caputo, R., Catalano, S., Monaco, C., Romagnoli, G., Tortorici, G. & Tortorici, L., 2010. Active faulting on the island of Crete (Greece), *Geophys. J. Int.,* **183**(1), 111–126.

Chaumillon, E. & Mascle, J., 1997. From foreland to forearc domains: new multichannel seismic reflection survey of the Mediterranean Ridge accretionary complex (Eastern Mediterranean), *Mar. Geol.,* **138**(3), 237–259.

Chlieh, M. *et al.*, 2007. Coseismic Slip and Afterslip of the Great Mw 9.15 Sumatra-Andaman Earthquake of 2004, *Bull. seism. Soc. Am.,* **97**(1A), S152–S173.

Cooper, F.J., Roberts, G.P. & Underwood, C.J., 2007. A comparison of 10^3–10^5 year uplift rates on the South Alkyonides Fault, central Greece: Holocene climate stability and the formation of coastal notches, *Geophys. Res. Lett.,* **34**(14), L14310, doi:10.1029/2007GL030673.

Copley, A., 2014. Postseismic afterslip 30 years after the 1978 Tabas-e-Golshan (Iran) earthquake: observations and implications for the geological evolution of thrust belts, *Geophys. J. Int.,* **197**(2), 665–679.

DeMets, C., Gordon, R.G.R. & Argus, D.D.F., 2010. Geologically current plate motions, *Geophys. J. Int.,* **181**(1), 1–80.

Dziewonski, A.M., Chou, T.-A. & Woodhouse, J.H., 1981. Determination of earthquake source parameters from waveform data for studies of global and regional seismicity, *J. geophys. Res.,* **86,** 2825–2852.

Ekström, G., Nettles, M. & Dziewoński, A., 2012. The global CMT project 2004–2010: Centroid-moment tensors for 13,017 earthquakes, *Phys. Earth planet. Inter.,* **200–201,** 1–9.

Emery, K., Heezen, B.C. & Allan, T., 1966. Bathymetry of the eastern Mediterranean Sea, *Deep Sea Res. Oceanogr. Abstr.,* **13**(2), 173–192.

Engdahl, E.R., van der Hilst, R. & Buland, R., 1998. Global teleseismic earthquake relocation with improved travel times and procedures for depth determination, *Bull. seism. Soc. Am.,* **88,** 722–743.

England, P., Howell, A., Jackson, J. & Synolakis, C., 2015. Palæotsunamis and tsunami hazards in the Eastern Mediterranean, *Phil. Trans. R. Soc. Lond., A.,* in Press.

Evelpidou, N., Vassilopoulos, A. & Pirazzoli, P., 2012. Holocene emergence in Euboea island (Greece), *Mar. Geol.,* **295–298,** 14–19.

Farías, M., Comte, D., Roecker, S., Carrizo, D. & Pardo, M., 2011. Crustal extensional faulting triggered by the 2010 Chilean earthquake: the Pichilemu Seismic Sequence, *Tectonics,* **30,** TC6010, doi:10.1029/2011TC002888.

Farr, T.G. *et al.*, 2007. The Shuttle Radar Topography Mission, *Rev. Geophys.,* **45,** doi:10.1029/2005RG000183.

Fitch, T.J., 1972. Plate convergence, transcurrent faults, and internal deformation adjacent to Southeast Asia and the western Pacific, *J. geophys. Res.,* **77**(23), 4432–4460.

Floyd, M.A. *et al.*, 2010. A new velocity field for Greece: implications for the kinematics and dynamics of the Aegean, *J. geophys. Res.,* **115,** B10403, doi:10.1029/2009JB007040.

Gallen, S., Wegmann, K., Bohnenstiehl, D., Pazzaglia, F., Brandon, M. & Fassoulas, C., 2014. Active simultaneous uplift and margin-normal extension in a forearc high, Crete, Greece, *Earth planet. Sci. Lett.,* **398,** 11–24.

Gauthier, A., 1979. Contribution à l'étude néotectonique du domaine Egéen: l'île de Rhodes (Dodécanèse, Grèce), *PhD thesis,* Academie de Versailles, Université de Paris XI, Centre d'Orsay.

Guidoboni, E. & Comastri, A., 1997. The large earthquake of 8 August 1303 in Crete: seismic scenario and tsunami in the Mediterranean area, *J. Seismol.,* **1**(1), 55–72.

Hall, J., Aksu, A.E., Yaltırak, C. & Winsor, J.D., 2009. Structural architecture of the Rhodes Basin: a deep depocentre that evolved since the Pliocene at the junction of Hellenic and Cyprus Arcs, eastern Mediterranean, *Mar. Geol.,* **258**(1), 1–23.

Hanks, T.C. & Kanamori, H., 1979. A moment magnitude scale, *J. geophys. Res.,* **84**(B5), 2348–2350.

Hill, E.M. *et al.*, 2012. The 2010 Mw 7.8 Mentawai earthquake: Very shallow source of a rare tsunami earthquake determined from tsunami field survey and near-field GPS data, *J. geophys. Res.,* **117**(B6), B06402, doi:10.1029/2012JB009159.

Hsu, Y.-J. *et al.*, 2006. Frictional afterslip following the 2005 Nias-Simeulue earthquake, Sumatra., *Science,* **312**(5782), 1921–1926.

Huchon, P., Lybéris, N., Angelier, J., Le Pichon, X. & Renard, V., 1982. Tectonics of the hellenic trench: A synthesis of sea-beam and submersible observations, *Tectonophysics,* **86**(1–3), 69–112.

Huguen, C., Mascle, J., Chaumillon, E., Woodside, J.M., Benkhelil, J., Kopf, A. & Volkonskaïa, A., 2001. Deformational styles of the eastern Mediterranean Ridge and surroundings from combined swath mapping and seismic reflection profiling, *Tectonophysics,* **343**(1), 21–47.

Hunter, J.D., 2007. Matplotlib: A 2D graphics environment, *IEEE Comput. Sci. Eng.,* **9,** 99–104.

Jackson, J. & McKenzie, D., 1988. The relationship between plate motions and seismic moment tensors, and the rates of active deformation in the Mediterranean and Middle East, *Geophys. J.,* **93,** 45–73.

Kershaw, S. & Guo, L., 2001. Marine notches in coastal cliffs: indicators of relative sea-level change, Perachora Peninsula, central Greece, *Mar. Geol.,* **179**(3–4), 213–228.

Kontogianni, V.A., Tsoulos, N. & Stiros, S.C., 2002. Coastal uplift, earthquakes and active faulting of Rhodes Island (Aegean Arc): modeling based on geodetic inversion, *Mar. Geol.,* **186**(3–4), 299–317.

Korycansky, D.G. & Lynett, P.J., 2005. Offshore breaking of impact tsunami: the Van Dorn effect revisited, *Geophys. Res. Lett.,* **32**(10), L10608, doi:10.1029/2004GL021918.

Lambeck, K., 1995. Late Pleistocene and Holocene sea-level change in Greece and southwestern Turkey: a separation of eustatic, isostatic and tectonic contributions, *Geophys. J. Int.,* **122,** 1022–1044.

Lambeck, K. & Bard, E., 2000. Sea-level change along the French Mediterranean coast for the past 30 000 years, *Earth planet. Sci. Lett.,* **175**(3), 203–222.

Lambeck, K. & Purcell, A., 2005. Sea-level change in the Mediterranean Sea since the LGM: model predictions for tectonically stable areas, *Quat. Sci. Rev.,* **24**(18–19), 1969–1988.

Lay, T., Ammon, C.J., Kanamori, H., Kim, M.J. & Xue, L., 2011. Outer trench-slope faulting and the 2011 Mw 9.0 off the Pacific coast of Tohoku Earthquake, *Earth Planets Space,* **63**(7), 713–718.

Lay, T., Ye, L., Kanamori, H., Yamazaki, Y., Cheung, K.F., Kwong, K. & Koper, K.D., 2013. The October 28, 2012 Mw 7.8 Haida Gwaii underthrusting earthquake and tsunami: slip partitioning along the Queen Charlotte Fault transpressional plate boundary, *Earth planet. Sci. Lett.,* **375,** 57–70.

Le Pichon, X. *et al.*, 1979. From subduction to transform motion: a seabeam survey of the Hellenic trench system, *Earth planet. Sci. Lett.,* **44**(3), 441–450.

Liu-Zeng, J. *et al.*, 2009. Co-seismic ruptures of the 12 May 2008, Ms 8.0 Wenchuan earthquake, Sichuan: East–west crustal shortening on oblique, parallel thrusts along the eastern edge of Tibet, *Earth planet. Sci. Lett.,* **286**(3–4), 355–370.

Mahsas, A., Lammali, K., Yelles, K., Calais, E., Freed, A.M. & Briole, P., 2008. Shallow afterslip following the 2003 May 21, Mw 6.9 Boumerdes earthquake, Algeria, *Geophys. J. Int.,* **172**(1), 155–166.

Mascle, J., Cleac'h, A. & Jongsma, D., 1986. The eastern Hellenic margin from Crete to Rhodes: example of progressive collision, *Mar. Geol.,* **73**(1–2), 145–168.

McCaffrey, R., 1996. Slip partitioning at convergent plate boundaries of SE Asia, *Geol. Soc. London, Spec. Publ.,* **106**(1), 3–18.

McCaffrey, R. & Abers, G., 1988. *SYN3: A Program for Inversion of Teleseismic Body Wave Forms on Microcomputers,* IASPEI Softw. Libr.

McCaffrey, R., Zwick, P. & Abers, G., 1991. *SYN4 Program,* IASPEI Softw. Libr.

McKenzie, D., 1972. Active Tectonics of the Mediterranean Region, *Geophys. J. R. astr. Soc.,* **30**(2), 109–185.

McKenzie, D., 1978. Active tectonics of the Alpine—Himalayan belt: the Aegean Sea and surrounding regions, *Geophys. J. R. astr. Soc.,* **55,** 217–254.

Meier, T., Rische, M., Endrun, B., Vafidis, A. & Harjes, H.P., 2004. Seismicity of the Hellenic subduction zone in the area of western and central Crete observed by temporary local seismic networks, *Tectonophysics,* **383**(3), 149–169.

Middleton, T.A. & Copley, A.C., 2013. Constraining fault friction by reexamining earthquake nodal plane dips, *Geophys. J. Int.,* **196**(2), 671–680.

Nocquet, J.-M., 2012. Present-day kinematics of the Mediterranean: A comprehensive overview of GPS results, *Tectonophysics,* **579,** 220–242.

Okada, Y., 1985. Surface deformation due to shear and tensile faults in a half-space, *Bull. seism. Soc. Am.,* **75**(4), 1135–1154.

Ozawa, S., Nishimura, T., Suito, H., Kobayashi, T., Tobita, M. & Imakiire, T., 2011. Coseismic and postseismic slip of the 2011 magnitude-9 Tohoku-Oki earthquake., *Nature,* **475**(7356), 373–376.

Özbakır, A.D., Şengör, A., Wortel, M. & Govers, R., 2013. The Pliny–Strabo trench region: A large shear zone resulting from slab tearing, *Earth planet. Sci. Lett.,* **375,** 188–195.

Pirazzoli, P.A., Montaggioni, L.F., Saliege, J.F., Segonzac, G., Thommeret, Y. & Vergnaud-Grazzini, C., 1989. Crustal block movements from Holocene shorelines: Rhodes island (Greece), *Tectonophysics,* **170**(1–2), 89–114.

Pirazzoli, P.A., Laborel, J. & Stiros, S.C., 1996. Earthquake clustering in the eastern Mediterranean during historical times, *J. geophys. Res.,* **101**(B3), 6083, doi:10.1029/95JB00914.

Reilinger, R., McClusky, S., Paradissis, D., Ergintav, S. & Vernant, P., 2010. Geodetic constraints on the tectonic evolution of the Aegean region and strain accumulation along the Hellenic subduction zone, *Tectonophysics,* **488**(1–4), 22–30.

Reimer, P. & McCormac, F., 2002. Marine radiocarbon reservoir corrections for the Mediterranean and Aegean Seas, *Radiocarbon,* **44**(1), 159-–166.

Reimer, P. *et al.*, 2013. IntCal13 and Marine13 radiocarbon age calibration curves 0–50,000 years cal BP, *Radiocarbon,* **55**(4), 1869–1887.

Scholz, C.H., Aviles, C.A. & Wesnousky, S.G., 1986. Scaling differences between large interplate and intraplate earthquakes, *Bull. seism. Soc. Am.,* **76**(1), 65–70.

Shaw, B. & Jackson, J., 2010. Earthquake mechanisms and active tectonics of the Hellenic subduction zone, *Geophys. J. Int.,* **181**, 966–984.

Shaw, B. *et al.*, 2008. Eastern Mediterranean tectonics and tsunami hazard inferred from the AD 365 earthquake, *Nat. Geosci.,* **1**(4), 268–276.

Shaw, B., Jackson, J., Higham, T., England, P. & Thomas, A., 2010. Radiometric dates of uplifted marine fauna in Greece: Implications for the interpretation of recent earthquake and tectonic histories using lithophagid dates, *Earth planet. Sci. Lett.,* **297**(3–4), 395–404.

Siani, G., Paterne, M. & Arnold, M., 2000. Radiocarbon reservoir ages in the Mediterranean Sea and Black Sea, *Radiocarbon,* **42**(2), 271–280.

Sibson, R. & Xie, G., 1998. Dip range for intracontinental reverse fault ruptures: Truth not stranger than friction?, *Bull. seism. Soc. Am.,* **88**(4), 1014–1022.

Siddall, M., Rohling, E.J., Almogi-Labin, A., Hemleben, C., Meischner, D., Schmelzer, I. & Smeed, D.A. Others2003. Sea-level fluctuations during the last glacial cycle, *Nature,* **423**, 853–858.

Sieh, K., Ward, S.N., Natawidjaja, D. & Suwargadi, B.W., 1999. Crustal deformation at the Sumatran Subduction Zone revealed by coral rings, *Geophys. Res. Lett.,* **26**(20), 3141–3144.

Sivan, D., Lambeck, K., Toueg, R., Raban, A., Porath, Y. & Shirman, B., 2004. Ancient coastal wells of Caesarea Maritima, Israel, an indicator for relative sea level changes during the last 2000 years, *Earth planet. Sci. Lett.,* **222**(1), 315–330.

Stanley, D.J. & Warne, A.G., 1994. Worldwide initiation of holocene marine deltas by deceleration of sea-level rise, *Science,* **265**(5169), 228–231.

Stewart, I., 1996. Holocene uplift and palaeoseismicity on the Eliki fault, Western Gulf of Corinth, Greece, *Ann. Geophys.,* **39**(3), 575–588.

Stiros, S.C., 2010. The 8.5+ magnitude, AD365 earthquake in Crete: Coastal uplift, topography changes, archaeological and historical signature, *Quat. Int.,* **216**(1–2), 54–63.

Stiros, S.C. & Blackman, D.J., 2013. Seismic coastal uplift and subsidence in Rhodes Island, Aegean Arc: evidence from an uplifted ancient harbour, *Tectonophysics,* **611**, 114–120.

Szeliga, W., 2013. 2012 Haida Gwaii Quake: Insight Into Cascadia's Subduction Extent, *EOS, Trans. Am. geophys. Un.,* **94**(9), 85–86.

ten Brink, U., Twichell, D., Geist, E. & Chaytor, J., 2007. The current state of knowledge regarding potential tsunami sources affecting US Atlantic and Gulf Coasts, Tech. rep., USGS.

ten Veen, J.H. & Kleinspehn, K.L., 2002. Geodynamics along an increasingly curved convergent plate margin: late Miocene-Pleistocene Rhodes, Greece, *Tectonics,* **21**(3), 8–1–8–21.

ten Veen, J.H., Woodside, J.M., Zitter, T.A., Dumont, J.F., Mascle, J. & Volkonskaia, A., 2004. Neotectonic evolution of the Anaximander Mountains at the junction of the Hellenic and Cyprus arcs, *Tectonophysics,* **391**(1), 35–65.

Tichelaar, B.W. & Ruff, L.J., 1993. Depth of seismic coupling along subduction zones, *J. geophys. Res.,* **98**(B2), 2017–2037.

Tiryakioğlu, I., Floyd, M., Erdoğan, S., Gülal, E., Ergintav, S., McClusky, S. & Reilinger, R., 2013. GPS constraints on active deformation in the Isparta Angle region of SW Turkey, *Geophys. J. Int.,* **195**(3), 1455–1463.

Titov, V.V. & Synolakis, C.E., 1995. Modeling of breaking and nonbreaking long-wave evolution and runup using VTCS-2, *J. Waterw. Port, Coastal, Ocean Eng.,* **121**(6), 308–316.

Titov, V.V. & Synolakis, C.E., 1998. Numerical modeling of tidal wave runup, *J. Waterw. Port, Coastal, Ocean Eng.,* **124**(4), 157–171.

Titschack, J., Nelson, C.S., Beck, T., Freiwald, A. & Radtke, U., 2008. Sedimentary evolution of a Late Pleistocene temperate red algal reef (Coralligène) on Rhodes, Greece: correlation with global sea-level fluctuations, *Sedimentology,* **55**(6), 1747–1776.

Uluğ, A., Duman, M., Ersoy, S., Özel, E. & Avcı, M., 2005. Late Quaternary sea-level change, sedimentation and neotectonics of the Gulf of Gökova: Southeastern Aegean Sea, *Mar. Geol.,* **221**(1–4), 381–395.

Vernant, P., Reilinger, R. & McClusky, S., 2014. Geodetic evidence for low coupling on the Hellenic subduction plate interface, *Earth planet. Sci. Lett.,* **385**, 122–129.

Vigny, C. *et al.*, 2011. The 2010 Mw 8.8 Maule megathrust earthquake of Central Chile, monitored by GPS, *Science,* **332**(6036), 1417–1421.

Wells, D.L. & Coppersmith, K.J., 1994. New empirical relationships among magnitude, rupture length, rupture width, rupture area, and surface displacement, *Bull. seism. Soc. Am.,* **84**(4), 974–1002.

Wessel, P., Smith, W.H.F., Scharroo, R., Luis, J. & Wobbe, F., 2013. Generic mapping tools: improved version released, *EOS, Trans. Am. geophys. Un.,* **94**(45), 409–420.

Woodside, J., Mascle, J., Huguen, C. & Volkonskaïa, A., 2000. The Rhodes Basin, a post-Miocene tectonic trough, *Mar. Geol.,* **165**(1–4), 1–12.

Yolsal-Çevikbilen, S. & Taymaz, T., 2012. Earthquake source parameters along the Hellenic subduction zone and numerical simulations of historical tsunamis in the Eastern Mediterranean, *Tectonophysics,* **536–537**, 61–100.

Zwick, P., McCaffrey, R. & Abers, G., 1994. *MT5 Program,* IASPEI Softw. Libr.

SUPPORTING INFORMATION

Additional Supporting Information may be found in the online version of this paper:

Figure S1. Variation of absolute mifits at individual sites (shown by the letters on the map) where uplift was observed with dip and distance from the coast. Black lines show contours of overall RMS misfit for the same models. Fault length is fixed at 60 km, strike is 205° and slip vector is 115°. The fault ruptures from the surface to 40 km depth, and the SW end of the fault is constrained to lie on a bearing of 115° from Lindos (0 km along strike). Rake is fixed at 90°.

Figure S2. Illustration of trade-offs between slip, dip and distance of the fault from the coast. (a) shows the variation in best-fitting slip, with all parameters apart from dip and distance from the coast fixed. The fault is constrained to strike at 205°; rupture is from the surface to 40 km depth; the length of the fault is 60 km and the SW end is constrained to lie on a bearing of 115° from Lindos (0 km along strike). Rake is fixed at 90°.

Figure S3. Illustration of trade-offs between RMS misfit, distance of the fault from the coast and maximum depth of rupture. The fault is constrained to strike at 205° and dip at 40°; rupture is from the surface to the depth specified; the length of the fault is 60 km and the SW end is constrained to lie on a bearing of 115° from Lindos (0 km along strike). Rake is fixed at 90°.

Figure S4. Illustration of trade-offs between slip, dip and distance of the fault from the coast. (a) shows the variation in best-fitting slip, with all parameters apart from length and distance from the coast fixed. (b) shows variation in RMS misfit over the same region of parameter space. The fault is constrained to strike at 205° and dip at 60°; rupture is from the surface to 40 km and the SW end is constrained to lie on a bearing of 115° from Lindos (0 km along strike). Rake is fixed at 90°.

Figure S5. Variation of minimum RMS misfit with strike and dip, with horizontal azimuth of slip vector fixed at 195° and all other parameters free to vary within the limits in Table 1 (main text). Letters show the locations in parameter space of models G–I (Fig. 6, main text).

(http://gji.oxfordjournals.org/lookup/suppl/doi:10.1093/gji/ggv307/-/DC1).

Please note: Oxford University Press is not responsible for the content or functionality of any supporting materials supplied by the authors. Any queries (other than missing material) should be directed to the corresponding author for the paper.